Research Article | Vol. 30, No. 11 / 23 May 2022 / Optics Express 19300
Optics EXPRESS

Sub-Nyquist optical pulse sampling for photonic blind source separation

TAICHU SHI,[1] YANG QI,[1] WEIPENG ZHANG,[2] PAUL PRUCNAL,[2] JIE LI,[1] AND BEN WU[1,*]

[1]Department of Electrical and Computer Engineering, Rowan University, Glassboro, NJ 08028, USA
[2]Lightwave Communications Laboratory, Department of Electrical Engineering, Princeton University, Princeton, NJ 08544, USA
[*]wub@rowan.edu

Abstract: We propose and experimentally demonstrate an optical pulse sampling method for photonic blind source separation. The photonic system processes and separates wideband signals based on the statistical information of the mixed signals, and thus the sampling frequency can be orders of magnitude lower than the bandwidth of the signals. The ultra-fast optical pulses collect samples of the signals at very low sampling rates, and each sample is short enough to maintain the statistical properties of the signals. The low sampling frequency reduces the workloads of the analog to digital conversion and digital signal processing systems. In the meantime, the short pulse sampling maintains the accuracy of the sampled signals, so the statistical properties of the under-sampled signals are the same as the statistical properties of the original signals. The linear power range measurement shows that the sampling system with ultra-narrow optical pulse achieves a 30dB power dynamic range.

1. Introduction

The substantially increased use of radio frequency (RF) spectrum generates wireless interferences. With the emerging as well as the evolving technologies in wireless communication systems that seek for higher frequencies for large bandwidth, the congestion of RF spectrum does not only exist under 6GHz (sub-6), but also appears in higher frequencies. Blind source separation (BSS) has been proved to be an effective way to manage such interferences [1,2]. By using multiple-input and multiple-output (MIMO) receivers, the BSS system separates the signal of interest (SOI) from interferences without pre-known information of the signals [3,4]. Traditional BSS methods separates the mixed signals with digital signal processing (DSP). The digital methods achieve MHz to GHz bandwidth and require the pre-known carrier frequencies, so the bandpass signals can be converted to baseband signals for analog to digital conversion (ADC) and BSS. For signals with bandwidths beyond GHz range [5–8], the high data rates generate considerable amount of workload to both the ADC and DSP, and thus it is challenging to achieve real-time signal separation of wideband signals. More importantly, for passive users, such as radio telescope, the carrier frequencies of SOI are unknown and could range from a few MHz to 100GHz [9,10]. Therefore, a BSS system that is capable of processing ultra-wideband signals is needed for both the growing needs of bandwidth from active users and the requirement of passive users.

Photonic signal processing provides a bandwidth independent method for BSS [11]. By modulating the RF signals on optical carriers, THz bandwidth is available at optical communication bands (193THz) [12]. Photonic BSS has been recently implemented with photonic integrated circuit [13,14]. One of the key advantages of photonic BSS is that the signals are separated in an analog way without ADC. Only a very small portion of the signals needs to be digitized to measure the statistical properties of the mixed signals and thus calculate the de-mixing matrix. The sampling frequencies can be orders of magnitude smaller than the bandwidths of the mixed signals, which greatly reduces the workloads of ADC and DSP. To sample the ultra-wideband

#435282 https://doi.org/10.1364/OE.435282
Journal © 2022 Received 28 Jun 2021; revised 5 Sep 2021; accepted 9 Sep 2021; published 18 May 2022

Optics EXPRESS

signals (100GHz) at sub-Nyquist sampling rate, the major challenge is the sampling time, and it is impractical for the sampling circuit to achieve pico-second or femto-second sampling time with MHz or kHz sampling rate.

In this paper, we take advantage of the under-sampling properties of photonic BSS for wideband RF signal processing and modulate the RF signals on optical pulses that pre-sample the signals before ADC. By using a mode-locked laser, the optical pulse width is in the order of 100fs. The ultra-narrow optical pulses collect samples of the mixed signals. Only a tiny portion of the mixed signals ($1/10^2$ to $1/10^5$) is collected, which greatly reduces the workload of ADC and DSP, while each collected sample is short and thus accurate enough to represent the statistical information of the mixed signals. The DSP system calculates the de-mixing matrix based on the statistical information and controls the photonic circuit to separate the SOI from interferences with the de-mixing matrix.

The relationship between the optical pulse sampling and photonic BSS is similar to the relationship between the biopsy sample preparation and curative surgery. The biopsy (pulse sampling) collects samples for analysis (DSP) and curative surgery (BSS) is performed based on the analysis. Traditional digital BSS method digitizes the mixed signals at Nyquist sampling rate and works in a similar way as cutting the whole tissue off for sample analysis, which is not efficient and introduce extra workloads to both sample preparation and analysis. The ultra-fast optical pulses function as biopsy preparation. With a small portion of the mixed signals sampled for statistical analysis, the workloads of both sample preparation (ADC) and analysis (DSP) are reduced for real-time and ultra-wideband signal processing.

2. Principle and experimental setup

This section discusses the principle and the experimental setup of photonic BSS system with optical pulse sampling. Section 2.1 discusses the principle of photonic BSS, and shows that the system can separate the mixed signals with sampling frequency lower than the Nyquist sampling rate. Section 2.2 discusses the principle of optical pulse sampling.

2.1. Principle of blind source separation with undersampling

Figure 1 shows the schematic diagram of the photonic circuit that implement BSS algorithm. The photonic BSS system processes mixed signals from a MIMO receiver. The mixed signals are represented by:

$$\boldsymbol{X} = \boldsymbol{AS} \text{ or } \begin{bmatrix} x_1 \\ x_2 \end{bmatrix} = \begin{bmatrix} a_{11} & a_{12} \\ a_{21} & a_{22} \end{bmatrix} \begin{bmatrix} s_{soi} \\ s_{int} \end{bmatrix} \tag{1}$$

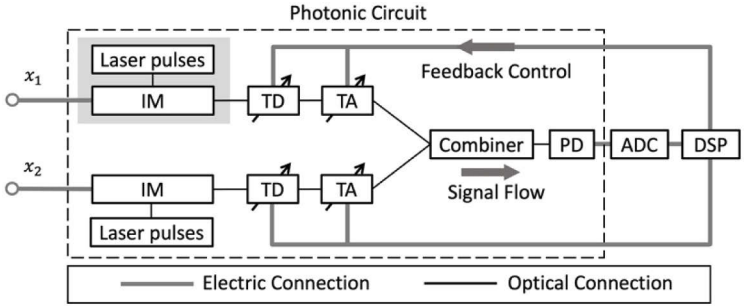

Fig. 1. Schematic diagram of the photonic BSS system (IM: optical intensity modulator, TD: tunable optical delay, TA: tunable optical attenuator, PD: photodetector, ADC: analog to digital conversion, DSP: digital signal processing).

Optics EXPRESS

$\boldsymbol{A}$ is the mixing matrix. x_1 and x_2 are received mixed signals from MIMO antennas. To demonstrate the principle of photonic BSS, a 16QAM is used as the SOI s_{soi}, and a Gaussian noise is used as the interference s_{int}. Both SOI and interference are baseband signals with the same bandwidth. Figure 2(a) is the scatter plot that shows the real parts of the mixed signals x_1 and x_2. The four straight lines match with the pattern of 16QAM, which corresponds to the projection of 16QAM on the real axis. Within each line, the density of the dots is Gaussian distributed, which represents the pattern of the interference. Separating SOI and interference is to find the de-mixing matrix $\boldsymbol{A}^{-1}$, which includes two steps, principal component analysis (PCA) and independent component analysis (ICA) [11]:

$$\boldsymbol{A}^{-1} = \boldsymbol{V}\boldsymbol{U}\boldsymbol{\Sigma}\boldsymbol{U}^{-1} \tag{2}$$

where $\boldsymbol{U}\boldsymbol{\Sigma}\boldsymbol{U}^{-1}$ represents the PCA, and $\boldsymbol{V}$ represents the ICA. To perform PCA, the 2nd order moments of the mixed signals are measured with different weights applied to the signals. By using the tunable attenuations in the photonic circuit (Fig. 1), the following weights are added to the mixed signals:

$$x_{PCA} = \cos(\theta)x_1 + \sin(\theta)x_2 \tag{3}$$

where θ is defined in Fig. 2. Based on Eq. (3), the 2nd order moment of x_{PCA} is a function of θ (red curve in Fig. 2(a)):

$$E(x_{PCA}^2) = q_1 + q_2\cos[2(\theta - \theta_0)] \tag{4}$$

where $E(x_{PCA}^2)$ is the time average of x_{PCA}^2. θ_0 shows the direction of first principal component. $q_1 + q_2$ is the magnitude of the first principle component, and $q_1 - q_2$ is the magnitude of the second principal component. The feedback control system changes the weights of the mixed signals by changing the attenuations. The weight changes are according to Eq. (3), where $\cos(\theta)$ and $\sin(\theta)$ are the weights. With three random θ values, the corresponding 2nd order moments of x_{PCA} are measured, and the three unknown parameters q_1, q_2, and θ_0 are determined. The PCA is performed with $\boldsymbol{X'} = [x_1', \ x_2'] = \boldsymbol{U}\boldsymbol{\Sigma}\boldsymbol{U}^{-1}\boldsymbol{X}$, where:

$$\boldsymbol{U} = \begin{bmatrix} \cos(\theta_0) & -\sin(\theta_0) \\ \sin(\theta_0) & \cos(\theta_0) \end{bmatrix} \tag{5}$$

$$\boldsymbol{\Sigma} = \begin{bmatrix} 1 & 0 \\ 0 & \sqrt{\frac{q_1+q_2}{q_1-q_2}} \end{bmatrix} \tag{6}$$

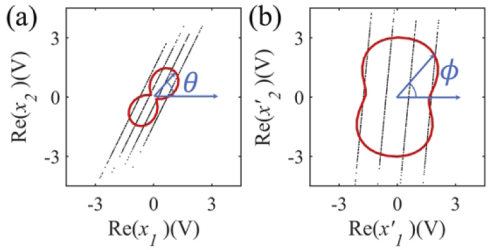

Fig. 2. (a) Real parts of the mixed signals, the red curve shows the 2nd order moments of the mixed signals; (b) Real parts of the mixed signals after PCA, the red curve shows the 4th order moments the mixed signals after PCA.

Optics EXPRESS

The PCA normalizes the 2nd order moments and whitens the mixed signals. To perform ICA, the 4th order moments (kurtosis) of the whitened signals are measured (red curve in Fig. 2(b)) with new weights applied:

$$x_{ICA} = \cos(\phi)x_1' + \sin(\phi)x_2' \tag{7}$$

$$E(x_{ICA}^4) = p_1 + p_2\cos[2(\phi - \phi_0)] + \ p_3\cos[4(\phi - \phi_0)] \tag{8}$$

where ϕ is defined in Fig. 2(b). With four random ϕ values, the unknown parameters p_1, p_2, p_3, and ϕ_0 are determined, and ICA can be performed with $\boldsymbol{S} = \boldsymbol{VX'}$, where:

$$\boldsymbol{V} = \begin{bmatrix} cos(\phi_0) & -sin(\phi_0) \\ sin(\phi_0) & cos(\phi_0) \end{bmatrix} \tag{9}$$

The de-mixing matrix is solved as $\boldsymbol{A^{-1}} = \boldsymbol{VU\Sigma U^{-1}}$. With the de-mixing matrix, the SOI is separated from the interference. The tunable delays and attenuators in Fig. 1 control the complex weights for x_1 and x_2 and the circuits within the dashed lines represent half of the de-mixing matrix $\boldsymbol{A^{-1}}$, which recovers the SOI. Based on Eq. (4) and Eq. (8), only statistical properties of the mixed signals are needed to find the de-mixing matrix $\boldsymbol{A^{-1}}$. To obtain the statistical properties, which are 2nd and 4th order moments, a sampling rate orders of magnitude lower than the Nyquist sampling rate can be applied. The undersampling rate reduces the workload of DSP, and the proposed system is able to process mixed signals with bandwidth that is beyond ADC speed limit.

2.2. Optical pulse sampling

When the sampling rate is orders of magnitude smaller than the Nyquist frequency, the duty cycle $/T_s$ also needs to be small enough, so the sampled signals can accurately represent the statistical information of the original signals. If the time duration of each sample is longer than the bit length of SOI, the sampled signals do not accurately represent the statistical information of the mixed signals. This can be explained by $E(x_1^2) \neq E(x_1)^2$, or in another word, when measuring the 2nd order moments, the time average of the square does not equal to the square of the time average. The sine function in Fig. 3(a) shows the maximum frequency of the mixed signal x_1. In a photonic BSS system, the sampling frequency ($1/T_s$) can be less than the frequency of the sine function, while the duration of each sample has to be small enough (τ_1 in Fig. 3(a)). If the duration of each sample (τ_2 in Fig. 3(a)) is comparable to T_s, each sample is an average of the changing signals, and the sampled signals cannot represent the distribution of the original signals.

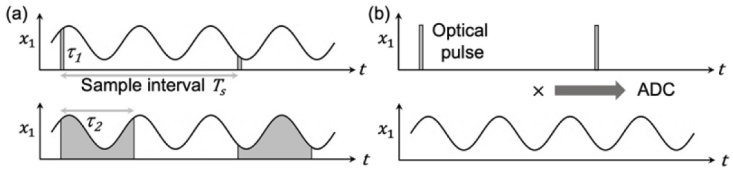

Fig. 3. (a) Comparison of short sampling time τ_1 and long sampling time τ_2 (b) Sample the signals with optical pulses

To obtain extremely small duty cycle (10^{-4} to 10^{-8}) for undersampling, the RF signals are modulated on a pulse laser that pre-samples the signals before ADC. The output of the optical modulator is the product of the periodic laser pulses and the RF signals (Fig. 3(b)). The sampling time is determined by the laser pulse width, so even ADC with long sampling time τ_2 is used afterwards; the sampled signals still represent accurate statistical information from the short sample duration τ_1.

Optics EXPRESS

3. Experimental results and analysis

In this section, optical pulse sampling for BSS is demonstrated with experimental results. The optical pulses are generated with both optical intensity modulator (section 3.1) and mode-locked laser (section 3.2). With optical intensity modulator, optical pulses sample RF signals with sub-6GHz frequencies. Such system can be used to separate multiple wireless systems that coexist at the same RF frequencies, including 4G LTE, weather radar, radio telescope, etc. With the mode-locked laser, since the pulse width of the mode-locked laser is in the order of 100fs, the power linearity is a key parameter of the ultra-narrow pulse for the sampling system. Section 3.2 investigates the power linear range of the receiver with femto-second pulses.

3.1. Demonstration of BSS with optical pulse sampling

In this section, we experimentally demonstrated that signals sampled with optical pulses accurately represent the statical properties. With 2^{nd} and 4^{th} order moments measured from the sampled signals, de-mixing matrix is solved. Figure 4 shows the basic concept of optical sampling with a binary signal. Figure 4(a) is the experimental setup of optical sampling for mixed signal x_1, and represents the setup marked with grey rectangle in Fig. 1. The same setup is used to sample mixed signal x_2, and the wavelengths of the continuous-wave lasers used to sample x_1 and x_2 are 1544nm and 1560nm respectively. For each laser, two intensity modulators are used. The first intensity modulator generates optical pulses and the second one modulates the RF signals on optical pulses. The sampled signals (Fig. 4(e)) are a product of the laser pulse sequence (Fig. 4(b)) and the unsampled signals (Fig. 4(d)). In this experiment, the laser pulse width is 5ns, and the signal bandwidth is 200MHz. Figure 4(c) is enlarged view of Fig. 4(b) and shows the width of the pulse is 5ns. Erbium-doped fiber amplifiers (EDFAs) are used to compensate the power loss introduced by intensity modulators. To demonstrate the principle of optical sampling with clear eye pattern, Figs. 4(d) and (e) only includes SOI, and interference is not introduced.

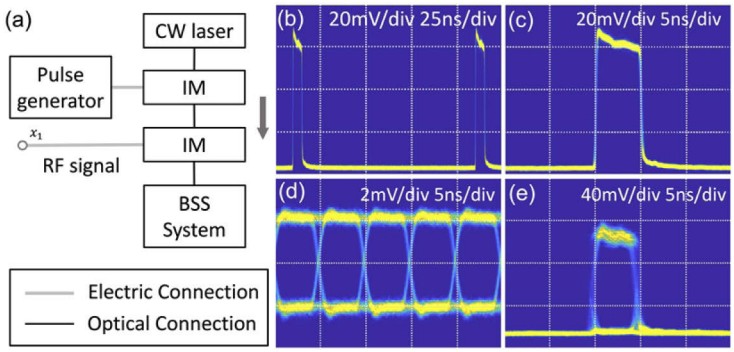

Fig. 4. Demonstration of optical sampling (a) Experimental setup for optical sampling (b) Laser pulse sequence (c) Enlarged view of (b) that shows the width of a pulse (d) Eye pattern of the original signals without pulse sampling (e) Sampled signals by laser pulses. (CW: continuous-wave).

In Fig. 5, Interference is introduced to demonstrate the effectiveness of the optical pulse sampling for BSS. Figures 5(a) and (b) show that the 2^{nd} order moments measured from pulse-sampled signals match with the theoretical results. The theoretical results calculate the 2^{nd} order moments with signals sampled at Nyquist frequency. In this experiment, the SOI s_{soi} is on-off keying none return to zero signal with random binary sequence. The data rate of SOI is 200Mbps, and the interference s_{int} is Gaussian noise with bandwidth overlapped with the bandwidth of SOI and clock unsynchronized with SOI. The mixing matrix (Eq. (1)) used in the experiment is $a_{11} = a_{22} = 1$, and $a_{12} = a_{21} = 0.5$. An arbitrary waveform generator is used to generate the

Optics EXPRESS

mixed signals x_1 and x_2. Figure 5(a) shows the x_1 and x_2 used in the experiment (black dots), and the theoretically calculated 2nd order moments (red curve). Each black dot is a sampled data point. The dots form the shape of two straight lines because the SOI is binary signal. Within each line, the dots are Gaussian distributed, which reflect the distribution of the interference. The six large black dots in Fig. 5(b) show the experimentally measured 2nd order moments in six different angles (θ in Eq. (3) and Fig. 2(a)). The black curve is the fitting result based on the experimental measurement. The fitting curve matches with the theoretical result (red curve). Figures 5(c) and (d) show the time domain signals measured with an oscilloscope and are used to calculate 2nd order moments in Fig. 5(b). Two points out of the six points are shown, and correspond to x_1, where $\theta = 0°$ (Fig. 5(c)), and x_2, where $\theta = 90°$ (Fig. 5(d)), respectively. In Fig. 5(b), the 2nd order moment of x_1 is significantly smaller than the 2nd order moment of x_2, which is also clearly shown in Figs. 5(c) and (d), where the variance of the signals in Fig. 5(c) is significantly smaller than the variance of the signals in Fig. 5(d).

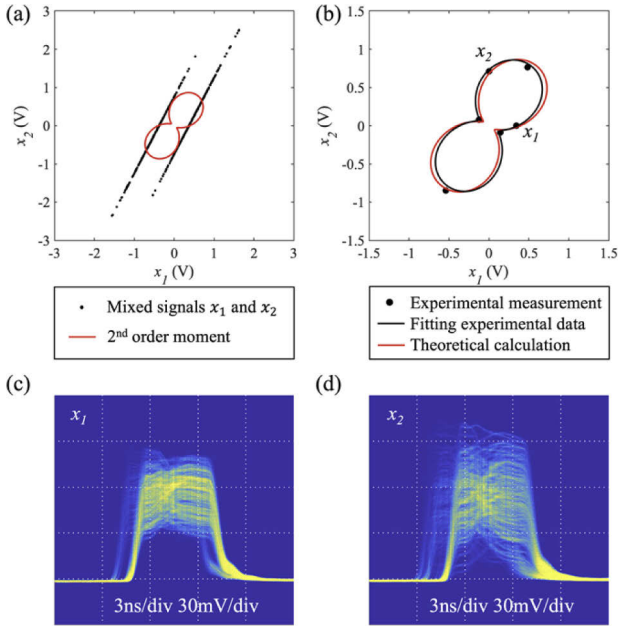

Fig. 5. Principal component analysis with signals sampled by optical pulses (a) Theoretical calculation of 2nd order moments (red curve) and scatter plot for the mixed signals x_1 and x_2 (black dots) (b) Comparison between theoretical calculation (red curve) and experimental measurement of 2nd order moments (black dots) (c) Experimentally measured histogram for x_1 (d) Experimentally measured histogram for x_2.

The de-mixing matrix is calculated with the pulse-sampled signals, and is applied to the mixed signals x_1 and x_2. Figure 6(a) shows that the recovered SOI matches with the original SOI, and a clear eye pattern is obtained Fig. 6(b). The pulse width in Figs. 6(a) and (b), or in another word, the duration of each sample is the same as the bit length of the original SOI. The bit error rate of the recovered signals is less than 1×10^{-9}. Figures 6(c) and (d) show that if the short optical pulse is not used, and the duration of each sample is five times the bit length of the SOI, the SOI is not separated with the Gaussian interference. The recovered SOI does not match with the original SOI (Fig. 6(c)) and a noisy eye pattern is obtained (Fig. 6(d)). The bit error rate is 9×10^{-2}, which is beyond the forward error correct limit [15].

To explain the results in Fig. 6, we test the system with 15 groups of signals, and each group includes a random binary SOI and a random Gaussian interference (Fig. 7). x_1' and x_2' in Fig. 7(a)

Optics EXPRESS

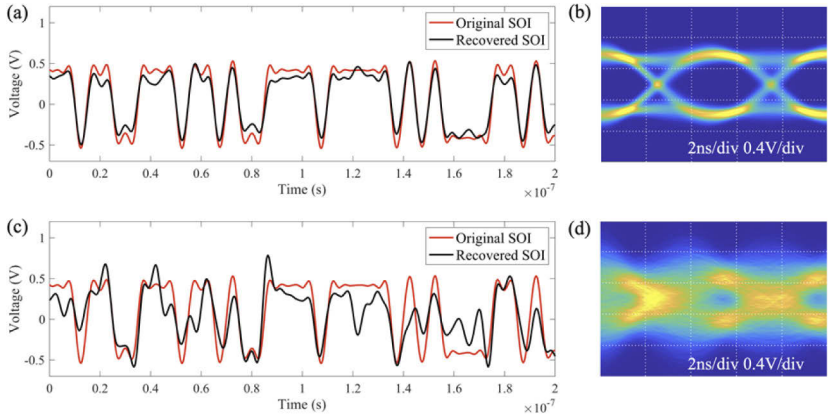

Fig. 6. Comparison of the recovered signals between short pulse sampling and long pulse sampling. The duration of each sample in (a) and (b) is the same as the SOI bit length. (a) shows the recovered SOI matches with the original SOI (b) shows a clear eye pattern. The duration of each sample in (c) and (d) is five times of the SOI bit length. (c) shows the recovered SOI does not match with the original SOI (d) shows a noisy eye pattern.

are the mixed signals after PCA. Based on Eq. (7) and (8), 4$^{\text{th}}$ order moments of x_1' and x_2' are calculated to perform ICA. The key parameter for ICA is ϕ_0 in Eq. (8). This is because in a scatter plot, matrix $\boldsymbol{V}$ (Eq. (9)) corresponds to rotate the scatter plot by an angle ϕ_0. If ϕ_0 is applied in a right way, the projections of the two lines on horizontal axis of the scatter plot does not have any overlaps (Fig. 7(b)), which means the SOI is completely separated from the interference. If ϕ_0 is not applied in a right way, the projections of the two lines on horizontal axis of the scatter plot have overlaps (Fig. 7(d)), which means the SOI is not completely separated from the interference. Figures 7(a) and (b) use short pulse sampling, where the duration of each sample is the same as the bit length of SOI. The ϕ_0, which is marked by red arrows in Fig. 7(a), from all the 15 groups of tests varies in a very small range (less than 10°). The projections of the rotated signals on the horizontal axis of the scatter plot does not have any overlaps (Fig. 7(b)). Figure 7(b) plots the rotated signals for 15 tests together, and each parallel line corresponds to one test. All the lines in Fig. 7(b) are close to each other with a variance of angle less than 10°. Figures 7(c) and (d) use long pulse sampling, where the duration of each sample is five times of the bit length of SOI. The ϕ_0 (red arrow in Fig. 7(c)) from 15 groups of tests varies in a large range (larger than 45°). The projections of the rotated signals on horizontal axis of the scatter plot have overlaps (Fig. 7(d)). Such overlaps result in bit errors and a noisy eye pattern (Fig. 6(d)).

Time jitter and clock synchronization analysis: In this experiment, the clock of the interference is not synchronized with the clock of the sampling pulses, which represent a general case where the clock of interference is unknown. Compared with traditional BSS methods based on DSP, the resistance to time jitter is an advantage of the photonic BSS. Clock synchronization is not necessary to solve the de-mixing matrix with the photonic BSS system. The photonic BSS system only needs to know the statical distribution of the received signal, and whether the sampled pulses are aligned with the clock of the received signals does not change the statistical distribution of the received signals. Clock synchronization is not needed for the photonic BSS process. Such advantage is especially important when the bandwidth and data rate of the interference is unknown.

Upper limit of the sampling interval: The optical pulse sampling system provides a sub-Nyquist sampling method for photonic BSS. The upper limit on the sampling interval depends on two factors: (1) the update rate of the de-mixing matrix f_{rate}. For mobile transmitter/receiver, the

Optics EXPRESS

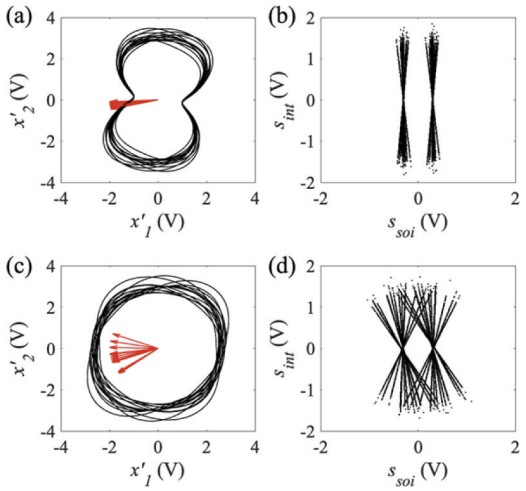

Fig. 7. Comparison of 4th order moments and the recovered signals between short pulse sampling and long pulse sampling. Both cases are tested with 15 groups of random signals. The duration of each sample in (a) and (b) is the same as the SOI bit length. (a) shows the 15 groups of random signals result in similar 4th order moments. (b) shows that all the 15 tests recover the SOI. The duration of each sample in (c) and (d) is five times of the SOI bit length. (c) shows the 15 groups of signals result in different and random 4th order moments. (d) shows that not all the 15 tests recover the SOI.

mixing matrix changes with the movement of the transmitter/receiver, and thus the de-mixing needs to update to follow the changes. (2) The number of samples collected N_{sample} to measure the distribution of the mixed signals. The upper limit of sampling interval is $1/f_{rate}N_{sample}$. For applications such as handhold wireless devices, the update rate f_{rate} is in the 0.1-1kHz range, and at least $N_{sample} = 1000$ samples are needed to measure the distribution. Therefore, the upper limit on the sampling interval is in the 1-10μs range.

3.2. Linearity analysis of mode-locked laser

Mode-locked laser generates femto-second laser pulses, which can be used to sample signals with 100GHz to THz bandwidth. Although femto-second pulses achieve the ultimate goal of ultra-fast sampling, the peak pulse power is orders of magnitude larger than its average power, and thus can saturate the photodetector of the BSS system (Fig. 1). By intensity modulating the RF signals on the laser pulses, the pulse power has to be within the linear range of the photodetector to perform effective signal processing. Both the measurement of 2nd and 4th order moments calculation and interference cancellation require the system to operate in the linear range. More importantly, the linear range determines the capability of the system to separate strong interference from weak SOI. The upper bound of the linear range is defined by the saturation power of the photodetector, and the lower bound of the linear range is defined by the noise-equivalent power. This section studies the saturation effect of the photodetector and the linear range of the sampling system with a mode-locked laser. Experimental results show that the linear range is at least 30dB, which means that the system is able to separate interference that is 30dB stronger than the SOI.

The mode-locked laser used in this experiment has a pulse width of 70fs (Fig. 8(b)), center wavelength of 1560nm, and a repetition rate of 37MHz (Precision Photonics FFL1560-MP [16]). The laser pulses are attenuated and then received with a photodetector with 50GHz bandwidth (Finisar XPDV21). The RF output of the photodetector is amplified by an RF amplifier with 9GHz bandwidth and then measured with an oscilloscope with 6GHz bandwidth (Keysight

Optics EXPRESS

6000X). Figure 8(a) shows the measured peak pulse voltage from the oscilloscope with the average power of laser scans from −45dBm to 0dBm. The average power is controlled by a digital tunable attenuator. The measured peak pulse voltage increases linearly with the average power and saturates at −10dBm. The saturation power of a photon detection system to the pulse laser can be calculated as [17]:

$$P_{sp} = P_{scw}\frac{t_p}{t_{FWHM}} \tag{10}$$

where the P_{sp} is the average power of the laser pulses that saturate the photodetector, P_{scw} is the power the continuous wave laser that saturates the photodetector, t_p is the pulse period, and the t_{FWHM} is the full width at half maximum of the system impulse response. The photodetector used in this experiment has a P_{scw} of 16dBm, the t_{FWHM} is measured to be 90ps (Fig. 8(c)). To measure the t_{FWHM} of the system, a 70fs pulse from the mode-locked laser can be treated as an impulse (70fs << 90ps). With P_{scw}, t_p, and t_{FWHM}, P_{sp} is calculated as −9dBm, which is close the measured saturation power −10dBm.

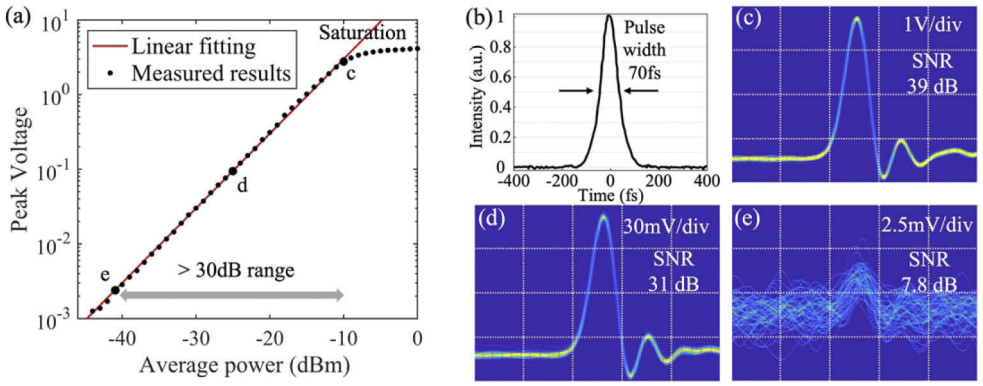

Fig. 8. (a) Peak voltage of the photodetector vs average power mode-locked laser, the small black dots are experimental results. (b) Femto-second pulse width measured with a correlator [16]. (c), (d) and (e) corresponds to points c, d, and e in (a), and are received pulses with average power of −10dBm, −25dBm, and −41dBm respectively. The time scales for (c), (d) and (e) are all 200ps/div.

The SNR at −10dBm average power is 39dB (Fig. 8(c)). The signal is defined as the peak voltage and the noise is defined as the variance of the signals at the peak. The SNR drops with the average power. The SNR is 31dB when the average power is −25dBm, and the SNR is 7.8dB when the average power is −41dBm, and the received histogram have observable pulse peak (Fig. 8(d)). The SNR is close to 1dB when the average power is −44dBm. The significant drop of SNR when then average power changes from −25dBm to −41dBm is based on the fact that the receiver noise is dominated by shot noise at relatively high signal power (average power from −25dBm to −10dBm) and is dominated by thermal noise at relatively low signal power (average power from −44dBm to −41dBm).

The pulse sampling system has a linear power range of over 30dB (−10dBm to −44dBm). The linear power range for the sampling system is important for BSS, since the separation of strong interference from weak SOI is a widely existing application scenario for the system. Such application requires the system to be able to address both the high and low power levels at the same time. The saturation power with continuous wave laser (P_{scw}) of the photodetector in this experiment is 16dBm. Without loss of generality, P_{scw} of the communication level photodetectors range from 10dBm to 27dBm, where a larger P_{scw} corresponds to a larger linear power range.

Optics EXPRESS

In addition to the 30dB range, we find that beyond the saturation power (−10dBm), the peak pulse voltage response of the photodetector still increases monotonously and significantly (Fig. 9). The results are repeatable, which means the photodetector does not break down. The significant increase of pulse voltage beyond −10dBm is not observed in Fig. 8(a), because it reaches maximum output power of the RF amplifier. To remove the saturation effect of RF amplifier, Fig. 9 is measured without RF amplifier and shows that although the output response of the photodetector is no longer linear beyond the saturation power of −10dBm, the peak voltage still increases significantly with the input average power and the SNR is over 40dB. Figure 9 shows the measured peak voltage with average power in both log scale (Fig. 9(a)) and linear scale (Fig. 9(b)). In the linear scale, the significant increase of peak voltage beyond saturation power (−10dBm or 0.1mW) is clearly shown. By calibrating the peak pulse voltage of the system, the nonlinear response can be corrected with the calibrated scale, and the −10dBm to 0dBm region can also be used to carry RF signals for BSS, which increase the dynamic range of the BSS system with another 10dB.

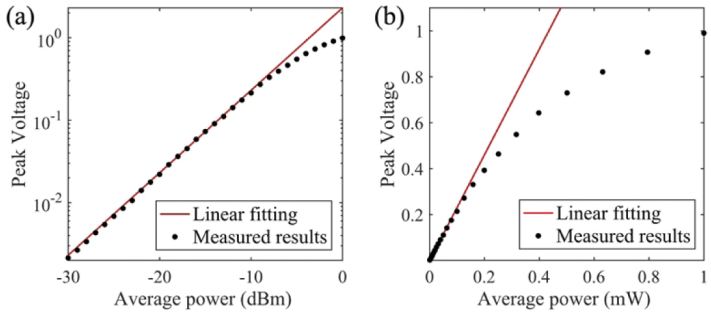

Fig. 9. Peak voltage of the received femto-second pulse vs average power without RF amplifier in (a) logarithmic scale and (b) linear scale

4. Conclusion

We proposed and experimentally demonstrated an optical pulse sampling system for photonic BSS. The photonic BSS separates the mixed signals in an analog way, and only statistical information of the mixed signals is needed to find the de-mixing matrix. The system is able to separate the SOI from interference at sampling rate orders of magnitude smaller than the data rate. The optical pulses sample the fast-changing signals for low-speed ADC without interference from adjacent bits. Experimental results show that with the pulse sampled signals, the statistical information can be accurately measured for BSS. By using femto-second pulses generated from mode-locked lasers, signals with bandwidth of 100GHz or more and power range of 30dB can be effectively sampled.

Funding. National Science Foundation (2128608); New Jersey Health Foundation (PC 77-21).

Acknowledgments. The authors would like to thank Yue-Kai Huang from NEC Laboratories America Inc for sharing the mode-locked laser for test and measurement in this paper.

Disclosures. The authors declare no conflicts of interest.

Data availability. Data underlying the results presented in this paper are not publicly available at this time but may be obtained from the authors upon reasonable request.

References

1. Z. Luo, C. Li, and L. Zhu, "A comprehensive survey on blind source separation for wireless adaptive processing: Principles, perspectives, challenges and new research directions," IEEE Access **6**, 66685–66708 (2018).

Optics EXPRESS

2. P. Y. Ma, A. N. Tait, W. Zhang, E. A. Karahan, T. Ferreira de Lima, C. Huang, B. J. Shastri, and P. R. Prucnal, "Blind source separation with integrated photonics and reduced dimensional statistics," Opt. Lett. **45**(23), 6494–6497 (2020).
3. T. R. Dean, M. Wootters, and A. J. Goldsmith, "Blind Joint MIMO Channel Estimation and Decoding," IEEE Trans. Inf. Theory **65**(4), 2507–2524 (2019).
4. Q. Guo, G. Ruan, and Y. Liao, "A time-frequency domain underdetermined blind source separation algorithm for MIMO radar signals," Symmetry **9**(7), 104 (2017).
5. R. W. Heath, N. Gonzalez-Prelcic, S. Rangan, W. Roh, and A. M. Sayeed, "An Overview of Signal Processing Techniques for Millimeter Wave MIMO Systems," IEEE J. Sel. Top. Signal Process. **10**(3), 436–453 (2016).
6. A. N. Uwaechia and N. M. Mahyuddin, "A comprehensive survey on millimeter wave communications for fifth-generation wireless networks: Feasibility and challenges," IEEE Access **8**, 62367–62414 (2020).
7. Y. Zhang and J. Mao, "An Overview of the Development of Antenna-in-Package Technology for Highly Integrated Wireless Devices," Proc. IEEE **107**(11), 2265–2280 (2019).
8. F. Liu, C. Masouros, A. P. Petropulu, H. Griffiths, and L. Hanzo, "Joint Radar and Communication Design: Applications, State-of-the-Art, and the Road Ahead," IEEE Trans. Commun. **68**(6), 3834–3862 (2020).
9. B. F. Burke, F. Graham-Smith, and P. N. Wilkinson, *An Introduction to Radio Astronomy* (Cambridge University Press, 2019).
10. R. Ekers and T. L. Wilson, "Radio telescopes," in *Planets, Stars and Stellar Systems: Volume 1: Telescopes and Instrumentation* (Springer, 2013).
11. A. N. Tait, P. Y. Ma, T. Ferreira De Lima, E. C. Blow, M. P. Chang, M. A. Nahmias, B. J. Shastri, and P. R. Prucnal, "Demonstration of Multivariate Photonics: Blind Dimensionality Reduction with Integrated Photonics," J. Lightwave Technol. **37**(24), C1 (2019).
12. B. J. Shastri, J. Chang, A. N. Tait, M. P. Chang, B. Wu, M. A. Nahmias, and P. R. Prucnal, "Ultrafast optical techniques for communication networks and signal processing," Springer Ser. Opt. Sci. **194**, 469–503 (2015).
13. P. Y. Ma, A. N. Tait, T. F. de Lima, C. Huang, B. J. Shastri, and P. R. Prucnal, "Photonic independent component analysis using an on-chip microring weight bank," Opt. Express **28**(2), 1827 (2020).
14. P. Y. Ma, A. N. Tait, T. F. de Lima, S. Abbaslou, B. J. Shastri, and P. R. Prucnal, "Photonic principal component analysis using an on-chip microring weight bank," Opt. Express **27**(13), 18329 (2019).
15. O. Gazi, *Forward Error Correction via Channel Coding* (Springer, 2019).
16. Data sheet for mode locked laser Precision Photonics FFL 1560-MP, http://www.tsukasa-tec.co.jp/documents/Catalog.pdf.
17. "Using High-Speed Photodetectors for Pulsed-Laser Measurements," Newport technical notes, https://www.newport.com/n/using-high-speed-photodetectors-for-pulsed-laser-measurements.